Letter

Decoding strong-field ionization of H_2 via photoelectron momentum torus

Daimu Ikeya,[1] Hikaru Fujise,[1] Minami Takahashi,[1] Kyoichiro Yasui,[1] Akitaka Matsuda,[1] Mizuho Fushitani,[1] Hirokazu Matsui,[2] Hiroka Hasegawa,[2] Oleg I. Tolstikhin,[3] Toru Morishita,[4,2] and Akiyoshi Hishikawa[1,5,*]

[1]*Department of Chemistry, Graduate School of Science, Nagoya University, Furo-cho, Chikusa, Nagoya, Aichi 464-8602, Japan*

[2]*Department of Engineering Science, The University of Electro-Communications, 1-5-1 Chofu-ga-oka, Chofu-shi, Tokyo 182-8585, Japan*

[3]*Moscow Institute of Physics and Technology, Dolgoprudny 141700, Russia*

[4]*Institute for Advanced Science, The University of Electro-Communications, 1-5-1 Chofu-ga-oka, Chofu-shi, Tokyo 182-8585, Japan*

[5]*Research Center for Materials Science, Nagoya University, Furo-cho, Chikusa, Nagoya, Aichi 464-8602, Japan*

(Received 19 April 2025; accepted 18 August 2025; published 12 September 2025)

Strong-field ionization of H_2 in circularly polarized laser fields (1035 nm, 35 fs, $\sim 1 \times 10^{14}$ W/cm^2) has been studied by three-dimensional electron-ion coincidence momentum imaging. Both the effective ionization potential and the applied laser electric field amplitude are simultaneously determined from the parameters characterizing the tunnel-electron torus in momentum space, using the adiabatic theory of strong-field ionization extended to include higher-order nonadiabatic effects as a reference. The effective ionization potential of H_2, obtained with an accuracy and precision of 10^{-2} a.u., reveals a clear shift from the field-free value. Dependence on both the field amplitude and the ionization pathways to H_2^+ and $H^+ + H$ is also resolved. These findings demonstrate that the target-specific properties can be quantitatively decoded from the structure of the photoelectron momentum torus, thus establishing a basis for quantitative ultrafast tunnel-electron spectroscopy.

DOI: 10.1103/g7g6-mm4z

Quantum barrier tunneling, a key manifestation of the wave nature of matter, plays a central role in modern science and technology. The scanning tunneling microscope (STM), for example, utilizes electron tunneling to provide a powerful method to study the properties of a single molecule on a surface, such as the energies of the molecular orbitals and their symmetries [1–3]. The electron tunneling also plays a pivotal role in atomic and molecular dynamics in strong laser fields ($\sim 10^{14}$ W/cm^2), such as higher-order harmonics generation, laser-induced electron diffraction, and Coulomb explosion, which serve as indispensable tools in modern ultrafast spectroscopy in atto- and femtosecond regimes [4–9].

In circularly polarized laser fields, the tunnel electron forms a torus (or donut)-like structure in the momentum space [Fig. 1(a)] [10–15]. The angular distribution along the major circle reflects the variation in the ionization yield by the direction of the electric fields applied to the molecule. This facilitates the assessment of the symmetries of the ionizing molecular orbitals as demonstrated in previous studies on H_2 [16], HCl [17], CO [18], OCS [19], CH_3I [20], and CF_4 [21].

The cross section of the torus, on the other hand, represents the photoelectron momentum distribution perpendicular to the instantaneous laser electric field at the tunneling. This transverse momentum distribution (TMD) also reflects target properties, including ionization potential, dipole, and polarizability, as well as the shape of molecular orbitals [22–30]. This suggests that the rich information on the target can be extracted from the photoelectron momentum distributions (PEMDs). However, this inherent feature of the tunneling ionization has not yet been fully explored. This is partly due to the difficulty in determining the applied electric field amplitude F with the required precision, as it depends on various characteristics of the laser pulse used to generate strong laser fields. The electric field is thus often treated as an adjustable parameter to interpret PEMDs, which hinders an accurate evaluation of the target properties. Another difficulty is located in the nonstatic nature of the laser fields. Contrary to the static field used in STM, the direction of the electric field rotates at the optical frequency ω in circularly polarized laser fields. The associated nonadiabatic effect introduces shifts in the transversal [31–36] and longitudinal [37–39] momenta.

Here, we demonstrate quantitative decoding of strong-field ionization of H_2 from photoelectron momentum torus formed in circularly polarized laser fields (1035 nm, 35 fs, $\sim 1 \times 10^{14}$ W/cm^2). We employ electron-ion coincidence momentum imaging using an electric field for charged-particle extraction [29], to precisely determine the PEMD parameters associated with different ionization pathways leading to H_2^+ or $H^+ + H$. Theoretically, the adiabatic theory of strong-field ionization [14,15] is extended to include higher-order strong-field and nonadiabatic corrections, yielding analytical expressions for the PEMD parameters. This framework enables the simultaneous determination of the ionization potential I_p and the electric field F from the observed momentum-space torus. We report the successful retrieval of effective ionization potentials of H_2 in strong laser fields with

*Contact author: hishikawa.akiyoshi.z6@f.mail.nagoya-u.ac.jp

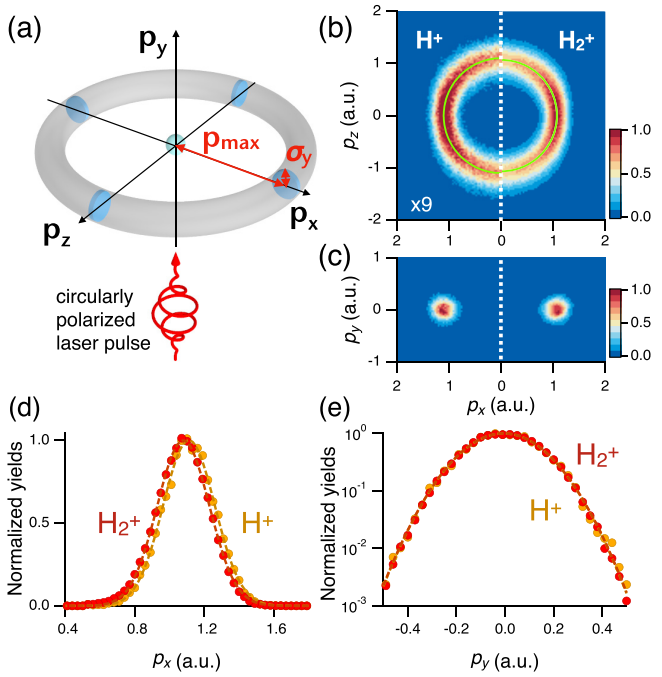

FIG. 1. (a) Schematic of photoelectron momentum distributions for tunneling ionization in circularly polarized strong laser fields, characterized by the major radius of the torus (p_{max}) and the width (σ_y) of the cross section (or transverse momentum distribution). (b) Typical laboratory-frame photoelectron momentum distributions recorded in coincidence with H^+ (left) and $H_2{}^+$ (right) in the p_x–p_z plane ($|p_y| \leqslant 0.1$ a.u.) at a wavelength of 1035 nm. The momentum of the maximum distribution (p_{max}) of the each torus is shown with a solid circle. (c) Same as panel (b) but in the p_x–p_y plane ($|p_z| \leqslant 0.1$ a.u.). (d) Photoelectron distributions along the p_x axis obtained from the momentum distribution in panel (c), integrated over $-0.5 \leqslant p_y \leqslant 0.5$ a.u for $H_2{}^+$ (red) and H^+ (orange). The dashed lines are the results of the least-squares fittings to the Gaussian function. (e) Same as panel (d) but along the p_y axis obtained by integration over $0.5 \leqslant |p_x| \leqslant 2.0$ a.u.

an accuracy and precision of 10^{-2} a.u. The results reveal a clear shift in the effective I_p from the field-free value, as predicted by the previous theoretical studies [40,41], and further show that the ionization potential depends on the ionization pathways. Atomic units are used throughout the paper if not otherwise specified.

The experimental setup has been described elsewhere [21,29]. Briefly, circularly polarized femtosecond laser pulses (1035 nm, 35 fs, 10–50 kHz) with high ellipticity ($\varepsilon \geqslant 0.99$) are focused onto a molecular beam of H_2 by a concave mirror ($f = 75$ mm) inside a vacuum chamber. A static electric field is applied to extract and guide the ions and photoelectrons toward position-sensitive detectors (PSD, RoentDek HEX80). The flight tube is shielded by a μ-metal tube to suppress possible distortions by ambient magnetic fields. The three-dimensional momenta $\mathbf{p} = (p_x, p_y, p_z)$ of electrons are determined in the laboratory frame (defined as shown in Fig. 1) from their time of flight (t) and positions (x, y) at the detector. The electron arrival position at the PSD is calibrated by a metal mask attached in front of the detector. The setup enables a precise PEMD measurement in the $p_x - p_y$ plane [29]. A Ti:sapphire femtosecond laser system (800 nm, 40 fs, 1 kHz) is also employed to evaluate the nonadiabatic effects on the tunneling ionization.

In the adiabatic limit, where the field rotation is much slower than the electron motion, the photoelectron torus in Fig. 1(a) may be expressed as

$$P(\mathbf{p}) \propto \exp\left[-\frac{(p_\rho - p_{\max})^2}{\sigma_\rho^2} - \frac{p_y^2}{\sigma_y^2}\right], \tag{1}$$

where the plane of the circularly polarized field is placed on the $x - z$ plane with the propagation direction along the y axis and $p_\rho = \sqrt{p_x^2 + p_z^2}$. Figures 1(b) and 1(c) show the experimental PEMDs plotted on the $p_x - p_z$ and $p_x - p_y$ planes, respectively. The electrons recorded in coincidence with $H_2{}^+$ form a toruslike structure, as expected.

For a quantitative discussion, we focus on the distribution on the $p_x - p_y$ plane, which is free from degrading by the time resolution of PSD [29]. The p_x and p_y distributions in this plane are shown in Figs. 1(d) and 1(e), which are evaluated by the least-squares fitting to Gaussian functions to determine the torus parameters, p_{max} and σ_y in Eq. (1). The results obtained at different pulse energies are plotted in Fig. 2(a). Both parameters increase with increasing pulse energy.

In the adiabatic limit, these parameters are known to be given by [10,11]

$$p_{\max} = \frac{F}{\omega}, \tag{2}$$

$$\sigma_y = \sigma_\rho = \sqrt{\frac{F}{\varkappa}}\left(\equiv \sigma_0^{(0)}\right), \tag{3}$$

with $\varkappa = \sqrt{2I_p}$ and the angular frequency $\omega = 0.0440$ a.u. at 1035 nm. Equation (3) is valid in the weak-field limit, $F \ll \varkappa^3$. The weak-field asymptotic theory (WFAT) [22] was developed to incorporate the first-order corrections in F to TMD [23]. The TMD width for a hydrogenlike atom is approximately given as

$$\sigma_y = \sigma_\rho = \sigma_0^{(0)}\sqrt{1 - \frac{5F}{4\varkappa^3}}, \tag{4}$$

which describes well the TMD width of H_2 having a quasi-s orbital character ($1s\sigma_g$) (see Appendix).

The theoretical prediction in the adiabatic limit [Eqs. (2) and (4)] is plotted in Fig. 2(a). The subscripts in the label "$\sigma_0 p_0$" denote the order of the nonadiabatic corrections on σ_y and p_{max}. The vertical ionization potential $I_p = 0.60443$ a.u. at the equilibrium internuclear distance $R_e = 1.4011$ a.u. (see Fig. 3(a) and the Supplemental Material [42]) is adopted in the calculation. As seen in Fig. 2(a), the theoretical curve deviates systematically from the experimental results. A similar trend is also found at a different wavelength (800 nm, $\omega = 0.0569$ a.u.) in Fig. 2(b).

The origin of the deviation becomes clear when σ_y is plotted against ωp_{max} [Fig. 2(c)]. The theoretical curves $\sigma_0 p_0$ for the two different wavelengths coincide with each other in this plot, while the experimental results at the two wavelengths show clear differences. This signifies the importance of the nonadiabatic effect in tunneling ionization associated with the finite frequency ω of field rotation. The nonadiabatic effect appears as the shift of the TMD, which translates to the torus

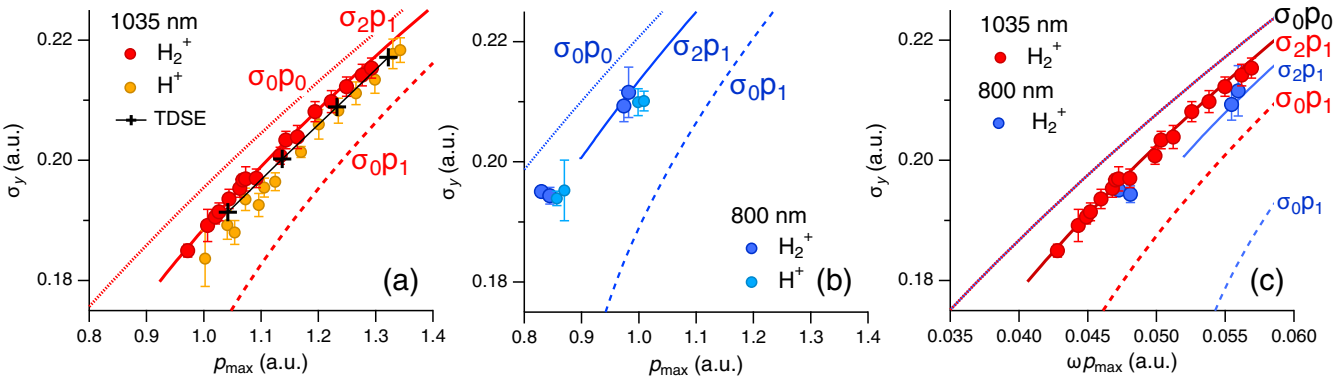

FIG. 2. (a) Width of transverse momentum distribution (σ_y) plotted against torus radius ($p_{\max}$) for H_2^+ and H^+ at the wavelength of 1035 nm. The theoretical results obtained by adiabatic and nonadiabatic theories for tunneling ionization ($I_p = 0.60433$ a.u.) and TDSE calculation (cross) are also shown for comparison. The subscripts, i and j, of the label "$\sigma_i p_j$" represent the order of nonadiabatic corrections on σ_y and $p_{\max}$, respectively. (b) Same as panel (a), but for the wavelength of 800 nm. (c) TMD width σ_y of H_2^+ plotted against $\omega p_{\max}$ at the wavelengths of 1035 and 800 nm.

radius $p_{\max}$ of PEMD [15,36,43]. Theoretically, $p_{\max}$ to the first order in ω is given by [12,13,15]

$$p_{\max} = \frac{F}{\omega} + \frac{\varkappa^2 \omega}{6F}, \tag{5}$$

which was later confirmed experimentally on Ne atoms using elliptically polarized laser fields [36]. Note that $p_{\max}$ in Eq. (5) has a minimum value of $2\varkappa/\sqrt{6}$, which occurs when the electric field amplitude F is equal to $\varkappa\omega/\sqrt{6}$. The theoretical curve ($\sigma_0 p_1$) incorporating the first-order nonadiabatic correction to $p_{\max}$ [Eq. (5)] shows a clear wavelength dependence, where the curve at 800 nm appears lower than that at 1035 nm. This is consistent with the experimental results, but substantial deviations in the absolute values are visible.

The nonadiabatic effects also appear in the TMD width. Here, we extend the adiabatic theory [14,15] to derive the following expression to the second order in ω (see Appendix):

$$\sigma_y = \sigma_0^{(1)}\left(1 + \frac{\varkappa^2\omega^2}{18F^2}\right). \tag{6}$$

When this second-order correction to σ_y [Eq. (6)] is introduced, the resultant curve ($\sigma_2 p_1$) reproduces well the experimental results at 800 and 1035 nm. Figure 2(a) also compares the theoretical curves with different orders of correction in the $\sigma_y - p_{\max}$ plane. While the validity of the nonadiabatic corrections is limited to qualitative assessment under the present conditions ($\omega/F \sim 1$), the good agreement with the experimental results suggests that the first few terms

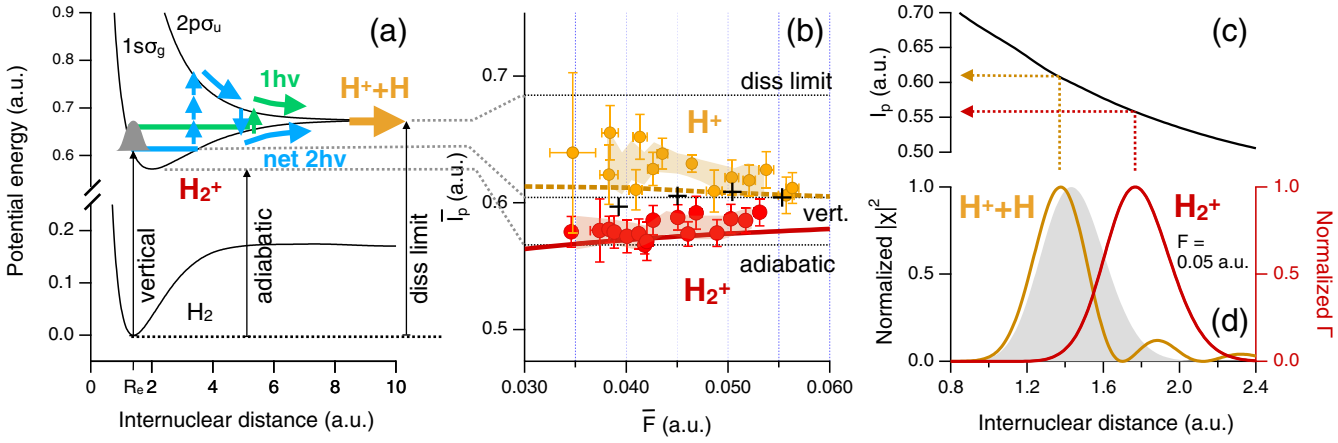

FIG. 3. (a) Potential energy curves of H_2 and H_2^+. (b) Ionization potential $\bar{I}_p$ plotted against the field amplitude $\bar{F}$ for H_2^+ (red) and H^+ (orange), where each point is shifted vertically by $-\delta I_p$ and horizontally by $-\delta F$. The results of the TDSE calculations (cross) are also plotted, showing that the simple parallel shift is sufficient to recover the I_p and F values used in the TDSE calculation (see the Supplemental Material [42]). The solid line shows the theoretical I_p by WFAT incorporating the nuclear motion effect. Results from the wavepacket calculation for H^+ are also shown (dashed line) (see text). (c) Ionization potential for fixed nuclei $I_p(R)$ obtained by potential energy curves of H_2 and H_2^+ ($1s\sigma_g$) plotted in panel (a). (d) Effective ionization rate $\Gamma_{\rm eff}(F,R) = \Gamma(F, I_p(R))|\chi_0(R)|^2$ at $F = 0.05$ a.u. (red) and the probability distribution $|\chi_0(R)|^2$ in the vibrational ground state of H_2 (gray). Also shown are the initial distribution subjected to the dissociation to $H^+ + H$ at the same field amplitude ($F = 0.05$ a.u.) (orange). Each curve is normalized by the peak value.

well describe the PEMD parameters of H_2 in this plot, where F acts as a parametric variable.

This proposes a unique method to determine both the effective field amplitude F and the ionization potential I_p simultaneously. *In situ* calibration of field amplitude was discussed previously using the simplest adiabatic formula [Eq. (2)] $F = \omega p_{\max}$ [44]. However, the accuracy is limited due to the nonadiabatic effect. To include the nonadiabatic correction in Eq. (5) to evaluate $p_{\max}$, *a priori* knowledge of $\varkappa$ or I_p is needed. This poses a significant challenge because the ionization potential should be evaluated in strong laser fields with a known F value. The difficulty can be overcome by using Eq. (6) for the TMD width incorporating the nonadiabatic effect. Since the TMD width σ_y is a function of $\varkappa$ and F, one can determine both of these parameters as a solution of Eqs. (5) and (6) with an observed set of the PEMD parameters $(p_{\max}, \sigma_y)$.

To evaluate the validity of this method, we first discuss the PEMD parameters obtained by numerical calculations solving the time-dependent Schrödinger equation (TDSE) (see Appendix). The PEMD parameters obtained for a single electron atom with the same $I_p = 0.60433$ a.u. are plotted in Fig. 2(a). The results obtained at four different field intensities show subtle differences from the corresponding analytical curves ($\sigma_2 p_1$). This can be attributed to higher-order nonadiabatic corrections neglected in Eqs. (5) and (6) and the non-Coulombic potential components neglected in the derivation of Eq. (4). Indeed, the effective ionization potential $\bar{I}_p$ and the effective field amplitude $\bar{F}$ derived from the four sets of the PEMD parameters $(p_{\max}, \sigma_y)$ show small deviations from I_p and F employed in the TDSE calculation. The differences are $\delta I_p = \bar{I}_p - I_p = 0.031(5)$ a.u. and $\delta F = \bar{F} - F = -0.0054(5)$ a.u., averaged over the four points, which should be taken into account in the following analysis of the experimental results.

Figure 3(b) shows $\bar{I}_p$ and $\bar{F}$ obtained from the experimental $(p_{\max}, \sigma_y)$ for $H_2{}^+$ at 1035 nm, where each point is shifted vertically by $-\delta I_p$ and horizontally by $-\delta F$. The resultant $\bar{I}_p$ appears in the range between the adiabatic and dissociation limits [see Fig. 3(a)], as expected. Interestingly, the determined $\bar{I}_p$ is smaller than the vertical ionization potential in the weak-field limit ($I_p = 0.60433$ a.u.). The reduction in the effective ionization potential can be interpreted in terms of the effect of the nuclear motion [40]. The tunneling ionization rate of H_2 can be expressed as $\Gamma_{\rm eff}(F, R) = \Gamma(F, I_p(R))|\chi_0(R)|^2$. Here, $\chi_0(R)$ is the vibrational wavefunction of H_2 at the internuclear distance R [Fig. 3(d)] and $\Gamma(F, I_p(R)) \propto \exp(-2\varkappa^3(R)/3F)$ is the field-dependent ionization rate. Since $I_p(R)$ is a decreasing function of R for H_2 as shown in Fig. 3(c), $\Gamma(F, I_p(R))$ increases rapidly as R increases. Therefore, the $\Gamma_{\rm eff}(F, R)$ distribution [40] peaks at R larger than R_e, as shown in Fig. 3(d). This explains the decrease in the effective ionization potential $\bar{I}_p$ from the vertical potential.

Recently, the nuclear motion effect has been incorporated in WFAT together with the effects of the core polarization and spectator nucleus [41]. The tunneling ionization rates derived for H_2 show excellent agreement with the full *ab initio* calculations [45]. Figure 3(b) plots the theoretical I_p [41] determined from the peak internuclear distance of $\Gamma_{\rm eff}(F, R)$ as a function of F, after being averaged over the parallel and perpendicular molecular alignment to the field direction. The experimental $\bar{I}_p$ determined with $H_2{}^+$ tends to show a gradual increase against $\bar{F}$ as predicted theoretically, which supports the importance of the effects of nuclear motion. The mean difference from the theoretical value is 0.014(1) a.u. with a standard deviation of 0.012(2) a.u., which estimates the accuracy and precision of the present tunnel-electron spectroscopy.

Figure 1 also shows the PEMD recorded in coincidence with the fragment ion H^+ formed by dissociative ionization of H_2 in the strong laser fields, $H_2 \rightarrow H^+ + H + e^-$. The p_x distribution peaks at a higher value than that of $H_2{}^+$, indicating that the difference in the ionization pathways is encoded in the PEMD parameters. Indeed, the $(p_{\max}, \sigma_y)$ plots for H^+ in Fig. 2(a) show small deviations from those of $H_2{}^+$. Similar shifts between $H_2{}^+$ and H^+ are also observed at the other wavelength of 800 nm, though the difference is on the order of the statistical uncertainty.

Figure 3(b) plots $\bar{I}_p$ obtained from the PEMD parameters for H^+, which show clear deviations from those obtained for $H_2{}^+$. The dissociative ionization of H_2 proceeds by postionization interaction with the laser fields. After ionization, the nuclear wavepacket evolves on the $1s\sigma_g$ potential and then fractionally dissociated via the photocoupling with the repulsive $2p\sigma_u$ state. It is established that the dissociation proceeds by the single-photon transition between these states, i.e., the "$1h\nu$" pathway or by the "net-$2h\nu$" pathway, associated with three-photon absorption and one-photon emission [46]. This suggests that H^+ is likely formed from the high vibrational levels of the $1s\sigma_g$ state, as shown in Fig. 3(a).

To understand how this dissociation process can contribute to the observed difference in the effective ionization potentials for $H_2{}^+$ and H^+, a nuclear wavepacket calculation in the two $H_2{}^+$ electronic states is performed. Figure 3(d) plots the initial wavepacket ($|\chi(R)|^2$) that undergoes the dissociation to $H^+ + H$ (see Appendix), exhibiting a peak shift from the original distribution ($|\chi_0(R)|^2$). This shows that $H_2{}^+$ formed at internuclear distances smaller than R_e are more prone to dissociation through the population to the high vibrational levels of $H_2{}^+$, which explains the large effective ionization potential compared to that of $H_2{}^+$.

Since multiphoton processes are involved, the relative contribution between the $1h\nu$ and net-$2h\nu$ pathways varies by the field intensity. This is confirmed by the experimental kinetic energy release spectra of the dissociative ionization (see the Supplemental Material [42]), showing that the net-$2h\nu$ component from the lower vibrational states becomes more prominent than the $1h\nu$ component as $\bar{F}$ increases. This would result in a decrease in the effective potential. Indeed, the experimental $\bar{I}_p$ for H^+ tends to decrease as $\bar{F}$ increases, which is consistent with the results of the wave-packet simulation plotted in Fig. 3(b) (see the Supplemental Material [42]). As far as we know, this is the first experimental demonstration to identify differences in the effective ionization potentials between the dissociative and nondissociative pathways for H_2 and other molecules in strong laser fields.

In summary, we have presented the first demonstration of quantitative decoding of strong-field ionization via photoelectron torus in momentum space. Both the effective ionization potentials and the laser electric field amplitudes are simul-

taneously extracted with the aid of the adiabatic theory of strong-field ionization. The difference in the ionization pathways to H_2^+ and $H^+ + H$ as well as their dependence on the electric field amplitude is securely captured. This shows that the target properties can be assessed from the tunnel-electron momentum distributions, thus establishing a robust framework for quantitative ultrafast tunnel-electron spectroscopy. Further theoretical development would facilitate a deeper understanding of laser tunneling ionization. In particular, more explicit treatment of the higher-order corrections and non-Coulombic potentials as well as the orbital character in $p_{\max}$ and σ_y would provide more accurate estimates of the effective potentials and the electric field amplitudes. This will allow for the application to quantitative visualization of ultrafast dynamics of general molecules [47,48], for example, with the angular streaking scheme in circularly polarized fields [49].

Acknowledgments. This work was supported by JSPS KAKENHI Grants No. JP22H00313, No. JP21K18929, No. JP19H00887, and No. JP16H04029, MEXT Quantum Leap Flagship Program (MEXT Q-LEAP) Grant No. JPMXS0118068681, and JST SPRING Grant No. JPMJSP2125. T.M. acknowledges support from JSPS KAKENHI Grant No. JP24K06916. O.I.T. acknowledges support from the Ministry of Science and Higher Education of the Russian Federation (No. FSMG-2023-0011). D.I. thanks the "Interdisciplinary Frontier Next-Generation Researcher Program of the Tokai Higher Education and Research System."

Data availability. The data that support the findings of this article are not publicly available upon publication because it is not technically feasible and/or the cost of preparing, depositing, and hosting the data would be prohibitive within the terms of this research project. The data are available from the authors upon reasonable request.

Appendix: Strong-field correction to PEMD. Equation (1) with the PEMD parameters $(p_{\max}, \sigma_y)$ given by Eqs. (2) and (3) holds in the adiabatic limit $\omega \to 0$. It was derived from the Keldysh theory [10,11] and hence holds only at sufficiently weak fields satisfying $F \ll \varkappa^3$. On the other hand, the adiabatic theory [14] expresses the PEMD in terms of the exact TMD in a static electric field [24], which eliminates the latter limitation. Here, we incorporate the first-order strong-field correction to Eq. (3) obtained on the basis of WFAT describing tunneling ionization in a static electric field [22]. Within WFAT(1) [23], which extends the weak-field asymptotics to the first-order terms in the field strength F, the TMD for tunneling ionization from the ground state of a hydrogenlike atom is given by

$$P(\mathbf{p}_\perp) = \frac{4\pi\varkappa}{F} W_{00}(F)|G_{00}|^2 e^{-s} \times \left[1 + \left(B_{00} + \frac{1}{4\varkappa^3}[6 - 4s - s^2]\right)F\right]. \quad \text{(A1)}$$

This equation describes the shape of the PEMD in the $p_x - p_y$ plane shown in Fig. 1(c) in the adiabatic limit. Here, $\mathbf{p}_\perp = (p_x - p_{\max}, p_y)$, $s = \varkappa p_\perp^2/F$, W_{00} and G_{00} are the field and structure factors for the dominant ionization channel [22], and B_{00} is a first-order correction coefficient accounting for the second-order Stark shift of the bound-state energy and the distortion of its unperturbed orbital [23]. The second term in the square brackets represents the first-order strong-field correction to the TMD. The terms including s contribute to the correction of the TMD width in Eq. (3). The effective TMD width is determined from the $1/e$ value of the distribution peak in Eq. (A1). Note that the resulting expression (4) is independent of B_{00} in the first-order approximation. The theoretical curve obtained with $\sigma_y = \sigma_0^{(0)}$ [Eq. (3)] significantly deviates from the experimental results (see the Supplemental Material [42]), which indicates the importance of the first-order correction in F in Eq. (4).

Nonadiabatic corrections to PEMD. Nonadiabatic effects in tunneling ionization are caused by finite nonzero values of ω in real experiments. The first-order correction appears as the shift of the transverse momentum distribution due to an increase of the radius $p_{\max}$ of the PEMD torus. This effect was predicted theoretically using the Keldysh theory [12,13] and, in more general context, using the adiabatic theory [15], and confirmed experimentally [36,43]. To the first order in ω, it is described by Eq. (5).

In the second order in ω, the width of the PEMD torus becomes affected. To take the higher-order nonadiabatic corrections into account, we use the adiabatic theory [14] equipped with a recently developed theory of Siegert states in a rotating electric field [50]. It follows from these theories that in a circularly polarized field of an arbitrary frequency, Eq. (1) takes the form

$$P(\mathbf{p}) \propto J_m^2(p_\rho F/\omega^2), \quad \text{(A2)}$$

where $J_m(x)$ is a Bessel function and

$$m = \frac{p^2 + (F/\omega)^2 + \varkappa^2}{2\omega}. \quad \text{(A3)}$$

By taking the asymptotics of Eq. (A2) in the region $\omega \ll F \ll \varkappa^3$ corresponding to the tunneling regime of ionization, we reproduce Eq. (5) and find

$$\sigma_y = \sigma_0^{(0)}\left(1 + \frac{1}{18} \times \frac{\varkappa^2\omega^2}{F^2}\right), \quad \text{(A4)}$$

$$\sigma_\rho = \sigma_0^{(0)}\left(1 + 0 \times \frac{\varkappa^2\omega^2}{F^2}\right). \quad \text{(A5)}$$

The second-order nonadiabatic correction in Eq. (A4) increases the width of the PEMD torus in the y direction. Including the strong-field correction from Eq. (4) into Eq. (A4) leads to Eq. (6). Note that the second-order nonadiabatic correction in Eq. (A5) appears with a zero coefficient. This means that nonadiabatic effects introduce an anisotropy in the cross section of the torus. In this paper, we do not discuss σ_ρ because it is affected by the pulse envelope.

[1] W. Ho, Single-molecule chemistry, J. Chem. Phys. **117**, 11033 (2002).

[2] J. Repp, G. Meyer, S. M. Stojković, A. Gourdon, and C. Joachim, Molecules on insulating films: Scanning-tunneling microscopy imaging of individual molecular orbitals, Phys. Rev. Lett. **94**, 026803 (2005).

[3] F. Schulz, M. Ijäs, R. Drost, S. K. Hämäläinen, A. Harju, A. P. Seitsonen, and P. Liljeroth, Many-body transitions in a single molecule visualized by scanning tunnelling microscopy, Nat. Phys. **11**, 229 (2015).

[4] P. B. Corkum and F. Krausz, Attosecond science, Nat. Phys. **3**, 381 (2007).

[5] M. F. Kling and M. J. Vrakking, Attosecond electron dynamics, Annu. Rev. Phys. Chem. **59**, 463 (2008).

[6] F. Krausz and M. Ivanov, Attosecond physics, Rev. Mod. Phys. **81**, 163 (2009).

[7] L. Gallmann, C. Cirelli, and U. Keller, Attosecond science: Recent highlights and future trends, Annu. Rev. Phys. Chem. **63**, 447 (2012).

[8] J. Xu, C. I. Blaga, P. Agostini, and L. F. DiMauro, Time-resolved molecular imaging, J. Phys. B **49**, 112001 (2016).

[9] F. Calegari, G. Sansone, S. Stagira, C. Vozzi, and M. Nisoli, Advances in attosecond science, J. Phys. B **49**, 062001 (2016).

[10] A. M. Perelomov, V. S. Popov, and M. V. Terent'ev, Ionization of atoms in an alternating electric field II, Sov. Phys. JETP **24**, 207 (1967).

[11] N. B. Delone and V. P. Krainov, Energy and angular electron-spectra for the tunnel ionization of atoms by strong low-frequency radiation, J. Opt. Soc. Am. B **8**, 1207 (1991).

[12] V. S. Popov, Tunneling and above-barrier ionization of atoms in a laser radiation field, J. Exp. Theor. Phys. **91**, 48 (2000).

[13] I. Barth and O. Smirnova, Nonadiabatic tunneling in circularly polarized laser fields: Physical picture and calculations, Phys. Rev. A **84**, 063415 (2011).

[14] O. I. Tolstikhin and T. Morishita, Adiabatic theory of ionization by intense laser pulses: Finite-range potentials, Phys. Rev. A **86**, 043417 (2012).

[15] M. Ohmi, O. I. Tolstikhin, and T. Morishita, Analysis of a shift of the maximum of photoelectron momentum distributions generated by intense circularly polarized pulses, Phys. Rev. A **92**, 043402 (2015).

[16] A. Staudte, S. Patchkovskii, D. Pavičić, H. Akagi, O. Smirnova, D. Zeidler, M. Meckel, D. M. Villeneuve, R. Dörner, M. Y. Ivanov, and P. B. Corkum, Angular tunneling ionization probability of fixed-in-space H_2 molecules in intense laser pulses, Phys. Rev. Lett. **102**, 033004 (2009).

[17] H. Akagi, T. Otobe, A. Staudte, A. Shiner, F. Turner, R. Dörner, D. M. Villeneuve, and P. B. Corkum, Laser tunnel ionization from multiple orbitals in HCl, Science **325**, 1364 (2009).

[18] J. Wu, L. P. H. Schmidt, M. Kunitski, M. Meckel, S. Voss, H. Sann, H. Kim, T. Jahnke, A. Czasch, and R. Dörner, Multiorbital tunneling ionization of the CO molecule, Phys. Rev. Lett. **108**, 183001 (2012).

[19] L. Holmegaard, J. L. Hansen, L. Kalhøj, S. Louise Kragh, H. Stapelfeldt, F. Filsinger, J. Küpper, G. Meijer, D. Dimitrovski, M. Abu-samha, C. P. J. Martiny, and L. B. Madsen, Photoelectron angular distributions from strong-field ionization of oriented molecules, Nat. Phys. **6**, 428 (2010).

[20] A. H. Winney, G. Basnayake, D. A. Debrah, Y. F. Lin, S. K. Lee, P. Hoerner, Q. Liao, H. B. Schlegel, and W. Li, Disentangling strong-field multielectron dynamics with angular streaking, J. Phys. Chem. Lett. **9**, 2539 (2018).

[21] H. Fujise, M. Uemura, H. Hasegawa, D. Ikeya, A. Matsuda, T. Morishita, L. B. Madsen, F. Jensen, O. I. Tolstikhin, and A. Hishikawa, Helicity-dependent dissociative tunneling ionization of CF_4 in multicycle circularly polarized intense laser fields, Phys. Chem. Chem. Phys. **24**, 8962 (2022).

[22] O. I. Tolstikhin, T. Morishita, and L. B. Madsen, Theory of tunneling ionization of molecules: Weak-field asymptotics including dipole effects, Phys. Rev. A **84**, 053423 (2011).

[23] V. H. Trinh, O. I. Tolstikhin, L. B. Madsen, and T. Morishita, First-order correction terms in the weak-field asymptotic theory of tunneling ionization, Phys. Rev. A **87**, 043426 (2013).

[24] V. N. T. Pham, O. I. Tolstikhin, and T. Morishita, Molecular Siegert states in an electric field. II. Transverse momentum distribution of the ionized electrons, Phys. Rev. A **89**, 033426 (2014).

[25] I. Petersen, J. Henkel, and M. Lein, Signatures of molecular orbital structure in lateral electron momentum distributions from strong-field ionization, Phys. Rev. Lett. **114**, 103004 (2015).

[26] V. N. T. Pham, O. I. Tolstikhin, and T. Morishita, Images of molecular orbitals in strong-field photoelectron momentum distributions generated by circularly polarized pulses, Phys. Rev. A **99**, 013428 (2019).

[27] I. Dreissigacker and M. Lein, Quantitative theory for the lateral momentum distribution after strong-field ionization, Chem. Phys. **414**, 69 (2013).

[28] C. Hofmann, T. Zimmermann, A. Zielinski, and A. S. Landsman, Non-adiabatic imprints on the electron wave packet in strong field ionization with circular polarization, New J. Phys. **18**, 043011 (2016).

[29] D. Ikeya, H. Fujise, S. Inaba, M. Takahashi, M. Yamamoto, T. Nakamura, Y. Nagao, A. Matsuda, M. Fushitani, and A. Hishikawa, Orbital effects on tunnel-electron momentum distributions: Ar and H_2 studied by electron–ion coincidence momentum imaging, J. Electron Spectrosc. Relat. Phenom. **262**, 147280 (2023).

[30] K. V. Bazarov and O. I. Tolstikhin, Generation of vortex electrons in tunneling ionization of polyatomic molecules: Exact results in the zero-range potential model, Phys. Rev. A **110**, 033107 (2024).

[31] L. Arissian, C. Smeenk, F. Turner, C. Trallero, A. V. Sokolov, D. M. Villeneuve, A. Staudte, and P. B. Corkum, Direct test of laser tunneling with electron momentum imaging, Phys. Rev. Lett. **105**, 133002 (2010).

[32] R. Boge, C. Cirelli, A. S. Landsman, S. Heuser, A. Ludwig, J. Maurer, M. Weger, L. Gallmann, and U. Keller, Probing nonadiabatic effects in strong-field tunnel ionization, Phys. Rev. Lett. **111**, 103003 (2013).

[33] S. Eckart, K. Fehre, N. Eicke, A. Hartung, J. Rist, D. Trabert, N. Strenger, A. Pier, L. P. H. Schmidt, T. Jahnke, M. S. Schöffler, M. Lein, M. Kunitski, and R. Dörner, Direct experimental access to the nonadiabatic initial momentum offset upon tunnel ionization, Phys. Rev. Lett. **121**, 163202 (2018).

[34] M. Li, M.-M. Liu, J.-W. Geng, M. Han, X. Sun, Y. Shao, Y. Deng, C. Wu, L.-Y. Peng, Q. Gong, and Y. Liu, Experimental verification of the nonadiabatic effect in strong-field ionization with elliptical polarization, Phys. Rev. A **95**, 053425 (2017).

[35] M.-M. Liu, M. Li, Y. Shao, M. Han, Q. Gong, and Y. Liu, Effects of orbital and Coulomb potential in strong-field

nonadiabatic tunneling ionization of atoms, Phys. Rev. A **96**, 043410 (2017).

[36] K. Liu, S. Luo, M. Li, Y. Li, Y. Feng, B. Du, Y. Zhou, P. Lu, and I. Barth, Detecting and characterizing the nonadiabaticity of laser-induced quantum tunneling, Phys. Rev. Lett. **122**, 053202 (2019).

[37] A. N. Pfeiffer, C. Cirelli, M. Smolarski, D. Dimitrovski, M. Abu-samha, L. B. Madsen, and U. Keller, Attoclock reveals natural coordinates of the laser-induced tunnelling current flow in atoms, Nat. Phys. **8**, 76 (2012).

[38] N. Teeny, E. Yakaboylu, H. Bauke, and C. H. Keitel, Ionization time and exit momentum in strong-field tunnel ionization, Phys. Rev. Lett. **116**, 063003 (2016).

[39] M. Li, H. Xie, W. Cao, S. Luo, J. Tan, Y. Feng, B. Du, W. Zhang, Y. Li, Q. Zhang, P. Lan, Y. Zhou, and P. Lu, Photoelectron holographic interferometry to probe the longitudinal momentum offset at the tunnel exit, Phys. Rev. Lett. **122**, 183202 (2019).

[40] O. I. Tolstikhin, H. J. Wörner, and T. Morishita, Effect of nuclear motion on tunneling ionization rates of molecules, Phys. Rev. A **87**, 041401(R) (2013).

[41] H. Matsui, O. I. Tolstikhin, and T. Morishita, Weak-field asymptotic theory of tunneling ionization of the hydrogen molecule including core polarization, spectator nucleus, and internuclear motion effects, Phys. Rev. A **103**, 033102 (2021).

[42] See Supplemental Material at http://link.aps.org/supplemental/10.1103/g7g6-mm4z for details.

[43] S. Eckart, M. Kunitski, M. Richter, A. Hartung, J. Rist, F. Trinter, K. Fehre, N. Schlott, K. Henrichs, L. P. H. Schmidt, T. Jahnke, M. Schöffler, K. Liu, I. Barth, J. Kaushal, F. Morales, M. Ivanov, O. Smirnova, and R. Dörner, Ultrafast preparation and detection of ring currents in single atoms, Nat. Phys. **14**, 701 (2018).

[44] A. S. Alnaser, X. M. Tong, T. Osipov, S. Voss, C. M. Maharjan, B. Shan, Z. Chang, and C. L. Cocke, Laser-peak-intensity calibration using recoil-ion momentum imaging, Phys. Rev. A **70**, 023413 (2004).

[45] T. C. Jagau, Coupled-cluster treatment of molecular strong-field ionization, J. Chem. Phys. **148**, 204102 (2018).

[46] P. H. Bucksbaum, A. Zavriyev, H. G. Muller, and D. W. Schumacher, Softening of H_2^+ molecular bond in intense laser fields, Phys. Rev. Lett. **64**, 1883 (1990).

[47] F. Calegari, D. Ayuso, A. Trabattoni, L. Belshaw, S. De Camillis, S. Anumula, F. Frassetto, L. Poletto, A. Palacios, P. Decleva, J. B. Greenwood, F. Martin, and M. Nisoli, Ultrafast electron dynamics in phenylalanine initiated by attosecond pulses, Science **346**, 336 (2014).

[48] T. Endo, A. Matsuda, M. Fushitani, T. Yasuike, O. I. Tolstikhin, T. Morishita, and A. Hishikawa, Imaging electronic excitation of NO by ultrafast laser tunneling ionization, Phys. Rev. Lett. **116**, 163002 (2016).

[49] P. Eckle, M. Smolarski, P. Schlup, J. Biegert, A. Staudte, M. Schöffler, H. G. Muller, R. Dörner, and U. Keller, Attosecond angular streaking, Nat. Phys. **4**, 565 (2008).

[50] T. K. Lindblom, O. I. Tolstikhin, and T. Morishita, Atomic Siegert states in a rotating electric field, Phys. Rev. A **104**, 023110 (2021).